Journal Pre-proof

Amorphous WO_{3-x} thin films with color characteristics tuned by the oxygen vacancies created during reactive DC sputtering

C. Guillén, J. Herrero

PII: S1005-0302(20)30999-3

DOI: https://doi.org/10.1016/j.jmst.2020.11.036

Reference: JMST 2721

To appear in: *Journal of Materials Science & Technology*

Received Date: 24 July 2020

Revised Date: 5 November 2020

Accepted Date: 9 November 2020

Please cite this article as: Guillén C, Herrero J, Amorphous WO_{3-x} thin films with color characteristics tuned by the oxygen vacancies created during reactive DC sputtering, *Journal of Materials Science and amp; Technology* (2020), doi: https://doi.org/10.1016/j.jmst.2020.11.036

Amorphous WO_{3-x} thin films with color characteristics tuned by the oxygen vacancies created during reactive DC sputtering

C. Guillén* and J. Herrero

Departamento de Energía (CIEMAT), Avda. Complutense 40, 28040 Madrid, Spain

* corresponding author, e-mail: c.guillen@ciemat.es

Graphical abstract

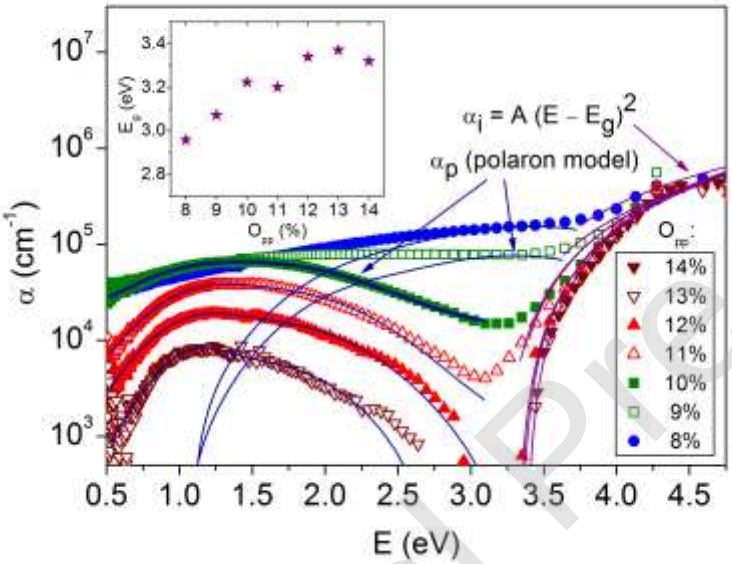

Highlights

- Amorphous WO_{3-x} is grown by DC sputtering, with x controlled by the oxygen pressure
- The most oxidized films show interband absorption at E_g = 3.37 eV and N ~ 10^{15} cm^{-3}
- For $0 < x \leq 0.2$, W^{5+} states increase absorption at 1.5 eV and the electron density
- For $x > 0.2$, W^{4+} states produce absorption at 3.3 eV but no higher electron density

Abstract

Tungsten oxides are interesting for a variety of applications due to their versatile optoelectronic characteristics, which can be tuned changing the composition and/or the crystalline structure. Coloration due to sub-bandgap absorption is often achieved by ion intercalation or doping in WO_3:M films (with M = H^+, Li^+, Na^+, etc. introducing extra electrons), but a more direct way is creating charged oxygen vacancies (V_O^+ and/or V_O^{2+}) in sub-stoichiometric WO_{3-x} forms. Here, amorphous WO_{3-x} thin films are obtained by reactive DC sputtering of a pure W target, on unheated glass substrates, changing the oxygen to argon pressures ratio. The control of intrinsic defects (oxygen vacancies and tungsten valence states) by the oxygen partial pressure allows tuning the morphology, sub-bandgap absorption and carrier density in these WO_{3-x} films, as it is proven by Raman spectroscopy, atomic force microscopy, optical spectrophotometry and Hall effect measurements.

Keywords: metal oxide; stoichiometry; optical absorption; electrical conductivity

1. Introduction

Tungsten oxides are used in a variety of energy-related applications, such as batteries [1], photocatalysis [2], optical shielding [3], and smart windows [4]. Their tunable optoelectronic properties, related to controlled composition deviations and various crystalline states (from amorphous to different crystallized phases) make them particularly attractive and special candidates for further development [5]. Stoichiometric WO_3 is a transparent oxide that generally crystallizes in tetragonal or hexagonal structures based on corner-sharing WO_6 octahedra, where each O^{2-} ion is bound to two W^{6+} ions in a linear configuration, represented as W^{6+}– O^{2-}–W^{6+} [4]. Coloration is often achieved by ion intercalation or doping in WO_3:M compounds (with M = H^+, Li^+, Na^+, etc. introducing extra electrons) [6], although a more direct way is to increase the electron concentration by creating charged oxygen vacancies (V_O^+ and/or V_O^{2+}) in sub-stoichiometric WO_{3-x} forms.

There are a number of crystalline WO_{3-x} phases constituted by edge-sharing octahedra [7], showing sub-bandgap absorption and metal-like characteristics [7,8], but a different coloration is identified in the amorphous material with respect to the crystalline one. Amorphous WO_{3-x} films grown at temperatures below 350 ºC have blue color due to a broad absorption band in the 1.3-1.5 eV range (depending on the preparation conditions), whereas the absorption shifts to lower energies (~ 0.7 eV) after crystallization at annealing temperatures near or above 400 °C [9–11]. In crystallized films, the coloration is attributed to Drude-like free electron absorption. Electrons can move freely in the crystal owing to the long-range order and the overlapping wave function of neighboring W sites [11]. In the amorphous material, electrons are localized at oxygen vacancies and transfer only to the closest W sites, reducing the W state and forming polarons there. The absorption is then

modeled by small polaron hopping between nearest-neighbor W sites with different valence states, although there are still some controversies about the states involved.

Some studies indicate that it is energetically advantageous to constitute a doubly charged vacancy with two W^{5+} ions [12,13], and the absorption of light arises by small polaron hopping from W^{5+} to W^{6+} sites [12]. Other authors consider that amorphous WO_{3-x} films include W^{6+} and W^{4+} states, being written as $(W^{6+})_{1-x}(W^{4+})_xO_{3-x}$ [14], and the chromic mechanism is based on the small polaron transition between W^{4+} and W^{5+} sites [14,15]. The competence of the two models is still in dispute, and the coexistence of both hopping mechanisms has also been proposed [16,17]. The absence of W^{5+} states in near-stoichiometric WO_3 precludes the optical absorption resulting from transitions between W^{5+} and other tungsten ions such as W^{6+} or W^{4+} [18]. Nevertheless, some oxygen-deficient films remain transparent, which supports the second model because W^{+6} and W^{+4} do not form polarons [14]. For defenders of the first model, this fact is explained by the formation of completely filled states associated with W^{5+}–W^{5+} pairs [13].

Among the various techniques used for the preparation of metal oxide films, reactive DC sputtering is especially suitable for large-scale manufacturing [4,5]. Amorphous WO_{3-x} layers have been obtained by DC sputtering from W or WO_3 targets at various oxygen and/or hydrogen flow rates [17–21]. In most cases, the as-grown films show high transparency and Raman characteristics that are typical of W^{6+} states, including W^{5+} features only after lithium intercalation (electrochromism) [18–20] or hydrogen spillover (gasochromism) [15,21]. This indicates that it is difficult to create charged oxygen vacancies during the growth process, due to the near-stoichiometric composition is favored in a large range of experimental conditions [22–24].

In the present work, the DC power and total pressure are adjusted to optimize the sputtering rate of a pure W target, while the oxygen partial pressure (O_{pp}) is varied to obtain

WO_{3-x} films with different x values on unheated glass substrates. The existence of several oxidation states (W^{6+}, W^{5+} and W^{4+}) is analyzed by Raman spectroscopy, optical and electrical measurements. The creation of charged oxygen vacancies (controlled by the O_{pp} during the sputtering process) is proven effective in modifying the surface roughness, sub-bandgap absorption and carrier density in these amorphous WO_{3-x} films.

2. Experimental procedure

Tungsten oxide layers were prepared on unheated soda-lime glass substrates by reactive DC magnetron sputtering from a W disc (purity 99.99%) of 15 cm in diameter. After evacuation of the chamber to a base pressure of 4×10^{-4} Pa, oxygen and argon gases were introduced by independent mass flow controllers, resulting in a change to a working pressure set at 0.4 Pa. Under these conditions, the application of a low power density (1.2 W/cm^2) has allowed minimizing the oxygen partial pressure needed to obtain stoichiometric WO_3 (O_{pp} ~ 14%) with a suitable deposition rate of 30 nm/min. Analogous rates are reported for higher power densities of about 10-18 W/cm^2, which require higher oxygen ratios (O_{pp} > 30%) to obtain WO_3 [22,23]. This is because the deposition rate increases as power increases, but also when the oxygen pressure decreases [19,23,24]. In our experimental setup, the variation of the oxygen pressure in the 8-14% O_{pp} range modifies the coloration of the sputtered layers, gradually changing from brown to dark blue, light blue, and transparent as the oxygen ratio increases.

The microstructure of the samples was analyzed with a B&W Tek system consisting of a BAC151B microscope and an i-Raman spectrometer, using a green laser of wavelength 532 nm as the excitation source. Crystallographic properties were examined by X-ray diffraction with radiation Cu Kα1 in a Philips X'pert instrument. Elemental compositions were obtained

by electron probe microanalysis in a JEOL JSM-6400 operating at 20 kV. The topography was examined by atomic force microscopy (AFM) with a Park XE-100, acquiring digital images to quantify the surface roughness.

The optical characterization used transmittance (T) and reflectance (R) measurements that were performed with a double beam spectrophotometer Perkin-Elmer Lambda 9 at wavelengths from 250 to 2500 nm, taking the air as reference. The transmittance was corrected for reflection losses, $Tc(\%) = 100\ T(\%)/(100 - R(\%))$, and the optical absorption coefficient was calculated as [22,23]: $\alpha = (1/t)\ \ln[100/Tc(\%)]$, including the film thickness value (t) obtained by profilometry with a Dektak 3030. The electrical conductivity, carrier concentration and mobility were determined with an ECOPIA Hall Measurement System.

3. Results and discussion

The evolution of color characteristics is illustrated in Figure 1 for tungsten oxide films that were prepared at different oxygen partial pressures, with a same thickness t = 150 nm. The samples grown at high oxygen ratios ($O_{pp} \geq 14\%$) are transparent in the visible and near-infrared regions, as expected for stoichiometric WO_3 [19,23]. Otherwise, the layers prepared at low oxygen pressures ($O_{pp} \leq 8\%$) have a brown appearance, due to a significant absorption in the visible range that is typical of WO_2 [23,25]. Between the two extreme situations, a gradual evolution of the optical characteristics (from light to dark blue colors) is achieved by controlling the oxygen partial pressure during the film growth. This indicates a change in intrinsic defects that can be tuned by the preparation conditions.

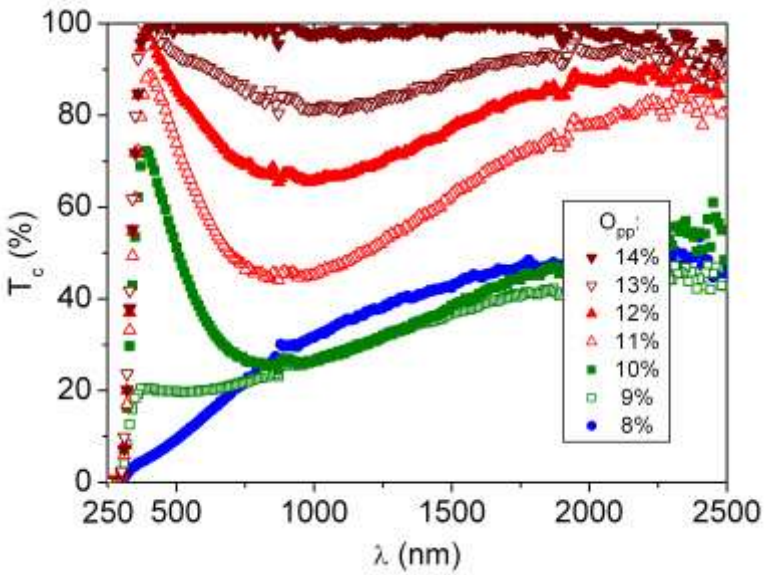

Figure 1. Transmittance spectra corresponding to WO_{3-x} thin films prepared at different oxygen partial pressures.

The proportion of oxygen vacancies in the layers is estimated from the composition data represented in Figure 2, taking the atomic ratio O/W = (3 – *x*) and then V_O (%) = 100 *x*/3 [26] for each WO_{3-x} sample. At high oxygen partial pressures, $O_{pp} \geq 14$ %, no significant oxygen vacancies ($x \leq 0.01$, $V_O \leq 0.3\%$) are found in the transparent films. By decreasing the oxygen pressure, the oxygen vacancies gradually increase from 2% ($WO_{2.95}$ obtained at 12% O_{pp}) to 12% ($WO_{2.65}$ at 8% O_{pp}). These composition data are in agreement with previous works that report blue color for WO_{3-x} layers with $0.1 < x < 0.4$ [17,22,24], while a brown appearance is observed for $x \sim 0.4$ [16], as for the current samples prepared at 8% O_{pp}.

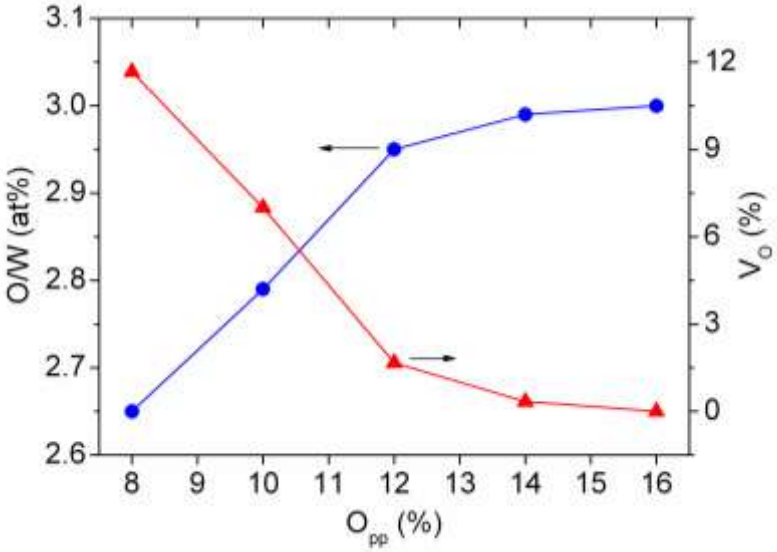

Figure 2. Evolution of the O/W atomic ratio and the oxygen vacancies proportion in WO_{3-x} films grown at different oxygen partial pressures.

These WO_{3-x} films are amorphous, which is verified by the absence of diffraction peaks in the XRD patterns measured for the various samples. Nevertheless, the Raman spectra represented in Figure 3 reveal significant differences in the microstructural characteristics of the layers depending on the oxygen content. The most oxidized films, prepared at O_{pp} = 13-14%, show a broad band centered at 820 cm^{-1}, which is related to the stretching of W^{6+}–O bonds in amorphous WO_3 [18,19], taking into account that the crystalline WO_3 evidences two distinct peaks in the 700-850 cm^{-1} range [1,11]. The peak at 360 cm^{-1} corresponds to the bending of W^{6+}–O bonds [1,27], while those observed at low frequencies (below 200 cm^{-1}) are attributed to lattice vibrational bands from $(W–O)_n$ blocks [27,28]. Otherwise, the relatively sharp peak at 930 cm^{-1} is due to the W^{6+}=O stretching mode of terminal oxygen atoms, which are predominant at the surface of clusters and nanovoids in amorphous and crystalline WO_3 films [18,19,28]. This mode disappears in the Raman spectra of the samples prepared at the lowest oxygen pressures, O_{pp} = 8-9%, where two additional peaks at 270 cm^{-1} and 790 cm^{-1} are assigned to the W^{4+}–O bending and stretching modes, respectively [30]. Besides, the intensity at 210 cm^{-1} originates from W^{5+}–W^{5+} species [13]. For the layers grown

in the intermediate oxygen region (10% ≤ O_{pp} ≤ 12%), Raman signals are more diffuse than in the extreme cases. This fact is related to the presence of several oxidation states (W^{6+}, W^{5+} and/or W^{4+}) that change the polarizability and thus the Raman intensity of the corresponding bonds [2]. Low frequency features have a relatively high intensity, similar to what observed in other sub-stoichiometric WO_{3-x} samples [31,32], and the presence of Raman bands around 400 cm^{-1} has been related to the W^{5+}–O bonds that generate film coloration after Li or H incorporation [18,20,33]. Therefore, the analysis in Figure 3 shows that charged oxygen vacancies created by sputtering are effective in producing W^{5+} and W^{4+} states controlled by the oxygen partial pressure.

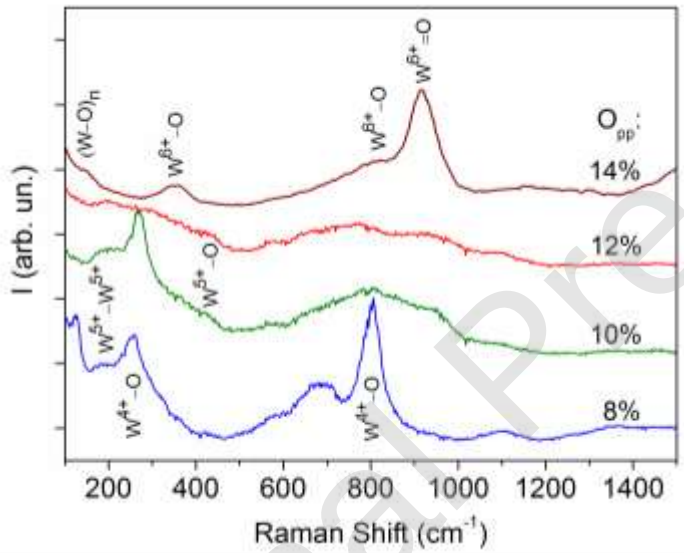

Figure 3. Raman spectra for the WO_{3-x} layers prepared at different oxygen partial pressures.

The surface morphology of the samples is illustrated in Figure 4, by representative AFM images on 2 μm x 2 μm areas. A line-scan taken in the middle of each image is included for comparison. The films are constituted by small grains, with average sizes increasing from 30 to 90 nm as the oxygen partial pressure decreases in the analyzed range. The root-mean-square roughness is around 2 nm for the layers prepared at low oxygen ratios (O_{pp} ≤ 9%) and it decreases below 1 nm when the oxygen pressure increases, in the same order than reported

for other sputtered films [19,34]. Analogous increase of the roughness with the grain size has also been observed in evaporated WO_3 layers [35].

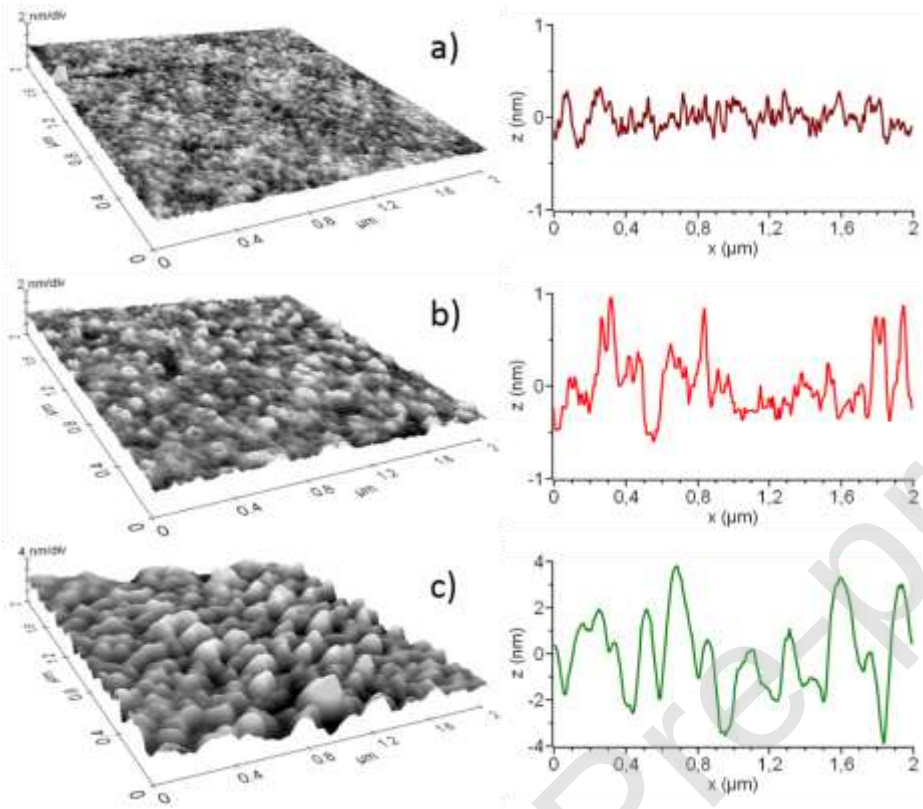

Figure 4. AFM images and representative line scans taken on the surface of WO_{3-x} layers prepared at different oxygen pressures: a) O_{pp}= 13%, b) O_{pp}= 11%, c) O_{pp}= 9%.

Figure 5 displays the absorption coefficient as a function of the illumination energy (α vs. E) for the films grown at different oxygen pressures. The sharp rise in α above 3.5 eV is due to interband transitions over the fundamental bandgap of tungsten oxide. In this region, the experimental data have been fitted to the expression $\alpha_i = A\ (E - E_g)^2$, which is typical of indirect transitions. The calculated bandgap energy is in the range E_g = 3.37-2.96 eV, decreasing as the oxygen content decreases. Analogous values were reported for other amorphous WO_{3-x} layers [23,24], generally higher than obtained for polycrystalline WO_{3-x} [27,34] and clearly superior to the 2.71 eV that corresponds to the indirect bandgap of WO_3 in

bulk [26]. Bandgap widening in disordered films has been attributed to quantum confinement, produced because the length over which the electrons are free to move is limited [12]. Otherwise, the relatively lower bandgap for layers with more oxygen deficiency is related to the inclusion of charged V_O states within or near the conduction band [36].

The most oxidized samples, prepared at $O_{pp} \geq 14\%$, show only absorption due to interband transitions. All other films have sub-bandgap absorption with a maximum at $E_{p1} \sim 1.5$ eV, which appears at 13% O_{pp} and increases as the oxygen ratio decreases down to 10% O_{pp}. Then, this peak reaches a saturation value at the same time that another peak is added at $E_{p2} \sim 3.3$ eV for 9% O_{pp}, which becomes more important for 8% O_{pp}. Analogous peaks, located at 1.4 and 3.3 eV, have been identified in Li_yWO_{3-x} layers, with different weight in the absorption spectra depending on the Li/W ratio [17]. By comparing theoretical and experimental data, the authors attribute the first peak to polaronic absorption due to $W^{5+} \leftrightarrow W^{6+}$ transitions, which achieves a maximum at Li/W = 0.5, and the second peak to $W^{4+} \leftrightarrow W^{5+}$ transitions, appearing when the intercalation level increases up to Li/W = 1.5 [17]. Therefore, sub-bandgap absorption is in accordance with the W^{5+} and W^{4+} states identified by Raman spectroscopy in the various WO_{3-x} samples, depending on the oxygen partial pressure.

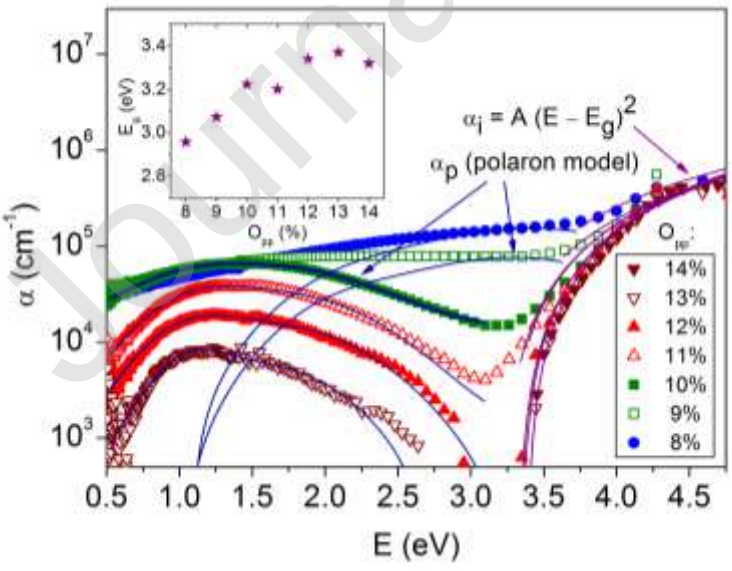

Figure 5. Absorption coefficients as a function of the radiation energy for WO_{3-x} films grown at different oxygen partial pressures. The lines represent fits according to an indirect interband transition (α_i) and the Brysin polaron model (α_p).

In band structure theory, polarons are technically treated as conduction band electrons accompanied by a spontaneous lattice deformation. This can be incorporated into the one-electron picture as levels splitting off the bottom of the conduction band as a result of the electron-phonon perturbation [37]. Polaronic absorption in the samples is generated by optical transitions between occupied and unoccupied states at the split levels, which can be described by the Brysin model used for Li_yWO_{3-x} films [38,39]. The model introduces a broad and asymmetric function that is proportional to the concentration of localization centers, the energy density of the polaronic ground states P(E), and that of the final states P(E´) [40]. Both densities, P(E) and P(E´), are well approximated by Gaussian functions, giving the absorption by small polarons [38]:

$$\alpha_p = A\, e^{-\frac{E_m{}^2}{\Gamma^2}}\, e^{-\frac{(E-4E_a)^2}{16E_akT}} + B\, e^{-\frac{E_m{}^2}{2\Gamma^2}}\, e^{-\frac{(E-4E_a-E_m)^2}{16E_akT+2\Gamma^2}} + C\, e^{-\frac{(E-4E_a)^2}{16E_akT+4\Gamma^2}} \qquad (1),$$

where E_m indicates the maximum of the density of states P(E) from the Fermi level, Γ is the bandwidth of the polaronic spectrum and E_a is the polaron hopping energy. The function exhibits an absorption maximum at $E_p \sim 4E_a + E_m$ [39], corresponding to $E_{p1} \sim 1.5$ eV and $E_{p2} \sim 3.3$ eV for the two peaks mentioned above. Figure 5 includes the fit of the experimental data to equation (1), performed in the sub-bandgap region for the various WO_{3-x} samples. In addition, Figure 6 shows the fitting parameters (E_m, E_a, and Γ) as a function of the oxygen partial pressure.

The distance from the maximum of P(E) to the Fermi level increases when the oxygen ratio decreases, within the range E_{m1}= 0.40-0.55 eV for the first peak attributed to $W^{5+} \leftrightarrow W^{6+}$ transitions and E_{m2} = 1.19-1.29 eV for the second peak due to $W^{4+} \leftrightarrow W^{5+}$ transitions. These

values are in agreement with those obtained for Li_yWO_3 layers, where they increased in the interval E_m = 0.2-1.2 eV as the Li/W proportion grew from 0.05 to 0.35 [38]. The increase in E_m is considered a result of electrons emanating from charged oxygen vacancies (or from charge balancing electrons inserted along with Li^+ species) and filling some of the previously empty band states, which makes the Fermi level gradually shifts upwards in energy when the oxygen deficiency increases [39]. Nevertheless, other studies have indicated that the P(E) distribution, but not the Fermi level, shifts with chemical composition [40]. The activation energy for small polaron hopping is E_{a1} = 0.27 ± 0.01 eV and E_{a2} = 0.53 ± 0.01 eV for the various samples, independent on the oxygen deficiency, as found in similar WO_{3-x} films [39]. The bandwidth enlarges in the range Γ = 0.47-0.70 eV when the oxygen deficiency increases, because a growing number of polaron states provides an extended distribution of polaron energies, as observed in Li_yWO_3 when the Li/W ratio increases [38].

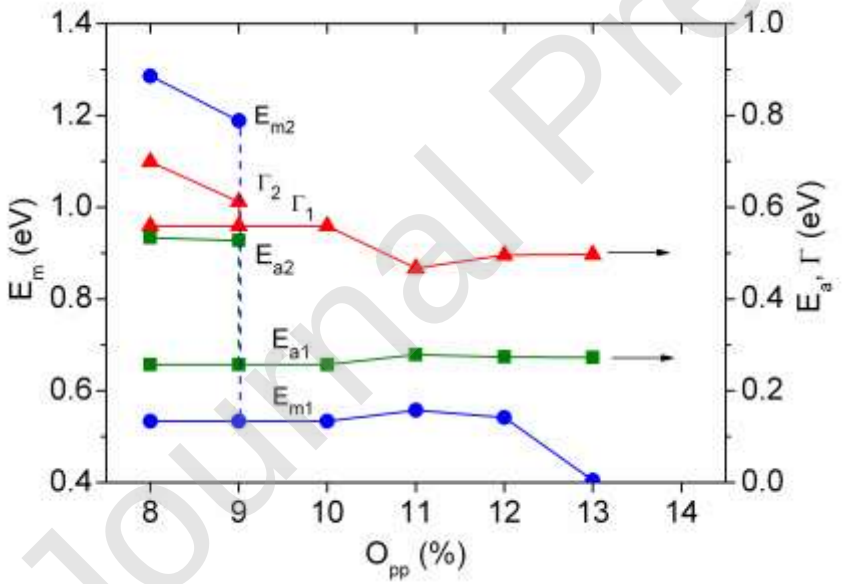

Figure 6. Parameters used to fit the sub-bandgap absorption to the Brysin polaron model, for WO_{3-x} films prepared at different oxygen partial pressures.

Electrical measurements of the samples are summarized in Figure 7, which shows that conductivity (σ) is dominated by the electron density (N), both increasing by several orders of magnitude when the oxygen partial pressure decreases. The mobility tends to decrease at high N values, but within a small range (μ = 0.4-17.3 cm^2/Vs) typical of amorphous films [41]. The most transparent layers, grown at O_{pp} = 13-14%, have low conductivities σ ~ 10^{-3} S/cm (with N ~ 10^{15} cm^{-3}) corresponding to stoichiometric WO_3 [41,42]. In the colored films, the conductivity increases as the oxygen partial pressure decreases, until it reaches a maximum of σ ~ 10^2 S/cm (with N ~ 10^{21} cm^{-3}) at $O_{pp} \leq 10\%$, which is according to the highest conductivity values obtained for sub-stoichiometric WO_{3-x} [26,41] and H_yWO_3 compounds [43]. The evolution of the optical and electrical characteristics corroborates the creation of charged oxygen vacancies acting as electron donors, which increase both the carrier concentration and the proportion of W^{5+} states responsible for the sub-bandgap absorption around 1.5 eV. Although W^{4+} states are also identified by additional absorption (around 3.3 eV) in the samples prepared at $O_{pp} \leq 9\%$, their contribution to conductivity is negligible. This is because the electrical transport is governed by the polaron hopping mechanism, making the conductivity inversely proportional to the activation energy [26,44], which is substantially higher for the W^{4+} states (E_{a2} = 0.53 eV) than for W^{5+} (E_{a1} = 0.27 eV), as shown in Figure 6.

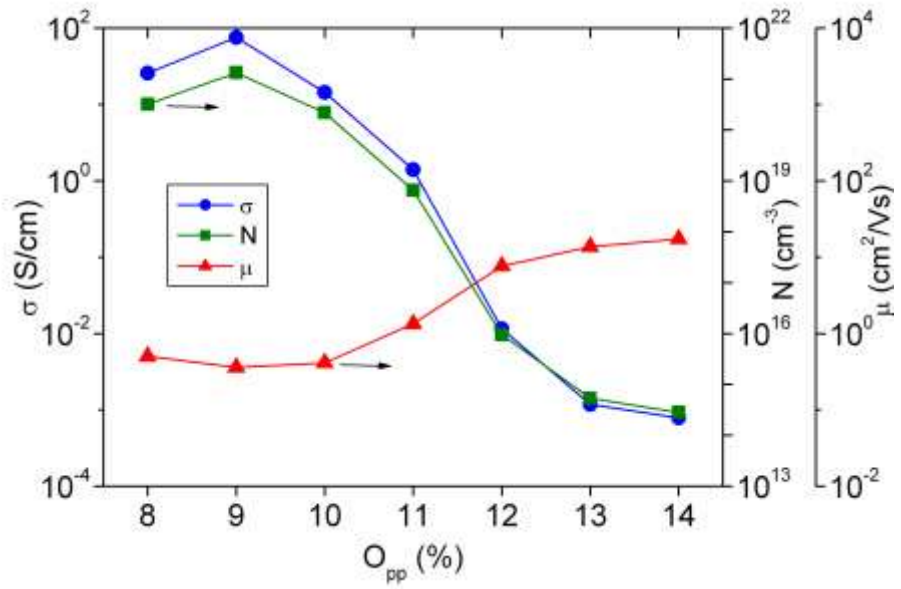

Figure 7. Electrical conductivity, carrier concentration and mobility for the WO_{3-x} films grown at different oxygen partial pressures.

The relation between blue color intensity (taken as α_{p1}, the absorption coefficient at E_{p1} ~ 1.5 eV) and layer composition has been quantified by several authors [45,46], finding a linear dependence from WO_3 with $\alpha_{p1} = 0$ up to $WO_{2.78}$ with $\alpha_{p1} = 1.0 \times 10^5$ cm^{-1} [46]. In this range, the sub-stoichiometric compound is considered a mixture of W^{5+} and W^{6+} states, $WO_{3-x} = (WO_{2.5})_c(WO_3)_{1-c}$, since α_{p1} is related to the W^{5+} concentration, $c = W^{5+}/(W^{5+} + W^{6+})$ [45]. Following these considerations, Figure 8 shows the c values obtained from the absorption data depicted in Figure 5. Saturation is achieved at $\alpha_{p1} = (6.8 \pm 0.3) \times 10^4$ cm^{-1}, corresponding to $c = 0.30 \pm 0.02$ for $O_{pp} \leq 10\%$, which agrees with the maximum sub-bandgap absorption reported in other works for WO_{3-x} [45], $H_{0.5}WO_3$ [47] and $Li_{0.5}WO_3$ [17]. At this point, assuming that the oxygen vacancies ($q = V_O$ obtained in Figure 1) only produce W^{5+} states, it would be:

$$WO_{3-x} = (W)_q(WO_3)_{1-q} = (WO_{2.5})_c(WO_3)_{1-c} \xrightarrow{yields} c = 6q \qquad (2),$$

whereas the production of W^{4+} states would give:

$$WO_{3-x} = (W)_q(WO_3)_{1-q} = (WO_2)_d(WO_3)_{1-d} \xrightarrow{yields} d = 3q \qquad (3).$$

Inclusion of these calculations in Figure 8 allows the comparison of compositional and optical data, showing that oxygen vacancies created in the range 12% ≥ O_{pp} ≥ 10% are effective in producing more W^{5+} than W^{4+} states, in a proportion W^{5+} ~ $4V_O$, but no more W^{5+} states appear at O_{pp} < 10% due to increasing competition of W^{4+} when V_O > 7%.

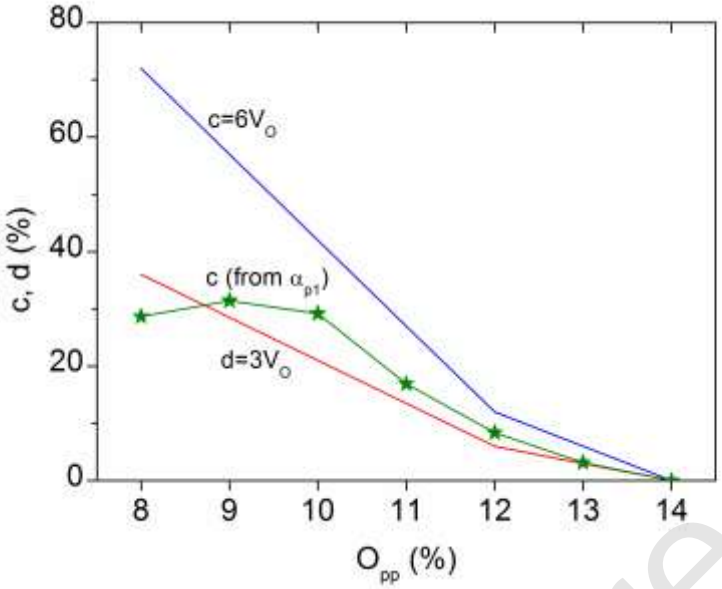

Figure 8. Concentration of W^{5+} states calculated from sub-bandgap absorption in comparison with the maximum concentration of W^{5+} or W^{4+} states deduced from the oxygen vacancies.

4. Conclusions

Amorphous WO_{3-x} thin films are obtained by reactive DC sputtering of a pure W target, changing intrinsic defects (oxygen vacancies and tungsten valence states) directly by the oxygen partial pressure, which allows tuning their morphological, optical and electrical characteristics in three different ranges.

At high oxygen pressures, O_{pp} ≥ 13%, no significant oxygen vacancies ($x \leq 0.01$, $V_O \leq$ 0.3%) are found in smooth films constituted by small grains, with average size ~ 30 nm. These layers show absorption due to indirect interband transitions with E_g = 3.37 eV, low

conductivity $\sigma \sim 10^{-3}$ S/cm and low electron density $N \sim 10^{15}$ cm^{-3}, corresponding to near-stoichiometric WO_3, as only W^{6+} states are identified by Raman spectroscopy.

The diminution of oxygen pressure in the interval $12\% \geq O_{pp} \geq 10\%$ allows increasing gradually oxygen vacancies $2\% \leq V_O \leq 7\%$ that produce W^{5+} states responsible for sub-bandgap absorption around 1.5 eV (α_{p1} that gives blue color) and increasing electron density. Saturation in the blue color intensity and electrical conductivity is achieved at $\alpha_{p1} = (6.8\pm0.3)x10^4$ cm^{-1}, $\sigma \sim 10^2$ S/cm (with $N \sim 10^{21}$ cm^{-3}) for $O_{pp} \leq 10\%$. Both the grain size and the surface roughness increase slightly with oxygen vacancies.

At lowest oxygen pressures, $O_{pp} < 10\%$, the oxygen vacancies continue increasing ($V_O > 7\%$) but no more W^{5+} states appear due to preferential formation of W^{4+}, as identified by Raman spectroscopy. These W^{4+} states are responsible for additional absorption around 3.3 eV (α_{p2} that gives brown color), but their contribution to conductivity is negligible. This is because the activation energy for the polaron hopping mechanism, determined from the fit of sub-bandgap absorption to the Brysin model, is higher for W^{4+} ($E_{a2} = 0.53$ eV) than for W^{5+} states ($E_{a1} = 0.27$ eV).

Declarations of interest: None.

Declaration of interests

☒ The authors declare that they have no known competing financial interests or personal relationships that could have appeared to influence the work reported in this paper.

Acknowledgments

This work has been carried out within the EFOX project.

References

[1] V. Lokhande, A. Lokhande, G. Namkoong, J.H. Kim, T. Ji, Results Phys. 12 (2019) 2012–2020.

[2] I.M. Szilágyi, B. Fórizs, O. Rosseler, Á. Szegedi, P. Németh, P. Király, G. Tárkányi, B. Vajna, K. Varga-Josepovits, K. László, A.L. Tóth, P. Baranyai, M. Leskelä, J. Catal. 294 (2012) 119–127.

[3] Y. Xin, H. Zhou, X. Ni, Y. Pan, X. Zhang, J. Zheng, S. Bao, P. Jin, RSC Adv. 5 (2015) 57757–57763.

[4] C.G. Granqvist, Thin Solid Films 564 (2014) 1–38.

[5] K. Thummavichai, Y. Xia, Y. Zhu, Prog. Mater. Sci. 88 (2017) 281–324.

[6] A. Hjelm, C.G. Granqvist, J.M. Wills, Phys. Rev. B 54 (1996) 2436–2445.

[7] D.B. Migas, V.L. Shaposhnikov, V.E. Borisenko, J. Appl. Phys. 108 (2010) 93714.

[8] D.B. Migas, V.L. Shaposhnikov, V.N. Rodin, V.E. Borisenko, J. Appl. Phys. 108 (2010) 93713.

[9] O.F. Schirmer, J. Electrochem. Soc. 124 (1977) 749–753.

[10] A. Deneuville, P. Gérard, J. Electron. Mater. 7 (1978) 559–588.

[11] E. Ozkan, S.H. Lee, C.E. Tracy, J.R. Pitts, S.K. Deb, Sol. Energy Mater. Sol. Cells 79 (2003) 439–448.

[12] G.A. De Wijs, R.A. De Groot, Phys. Rev. B 60 (1999) 16463–16474.

[13] G.A. De Wijs, R.A. De Groot, Electrochim. Acta 46 (2001) 1989–1993.

[14] J. Zhang, D.K. Benson, C.E. Tracy, S.K. Deb, A.W. Czanderna, C. Bechinger, J. Electrochem. Soc. 144 (1997) 2022–2026.

[15] M. Stolze, B. Camin, F. Galbert, U. Reinholz, L.K. Thomas, Thin Solid Films 409 (2002) 254–264.

[16] G.A. Niklasson, C.G. Granqvist, J. Mater. Chem. 17 (2007) 127–156.

[17] L. Berggren, J.C. Jonsson, G.A. Niklasson, J. Appl. Phys. 102 (2007) 1–7.

[18] S.-H. Lee, H.M. Cheong, C.E. Tracy, A. Mascarenhas, A.W. Czanderna, S.K. Deb, Appl. Phys. Lett. 75 (1999) 1541–1543.

[19] H.H. Lu, J. Alloys Compd. 465 (2008) 429–435.

[20] H.-C. Chen, D.-J. Jan, Y.-S. Luo, K.-T. Huang, Appl. Opt. 53 (2014) A321.

[21] M. Stolze, D. Gogova, L.K. Thomas, Thin Solid Films 476 (2005) 185–189.

[22] L. Berggren, G.A. Niklasson, Solid State Ionics 165 (2003) 51–58.

[23] S.H. Mohamed, H.A. Mohamed, H.A. Abd El Ghani, Phys. B Condens. Matter 406 (2011) 831–835.

[24] C. Li, J.H. Hsieh, M.T. Hung, B.Q. Huang, Vacuum 118 (2015) 125–132.

[25] M. Weil, W.-D. Schubert, ITIA Newsl. (2013) 1–12.

[26] G. Mattoni, A. Filippetti, N. Manca, P. Zubko, A.D. Caviglia, Phys. Rev. Mater. 2 (2018) 1–7.

[27] J.E. Flores-Mena, J. Díaz-Reyes, J.A. Balderas-López, Rev. Mex. Fis. 58 (2012) 504–509.

[28] Y. Djaoued, S. Balaji, R. Brüning, J. Nanomater. 2012 (2012).

[29] S. Poongodi, P.S. Kumar, Y. Masuda, D. Mangalaraj, N. Ponpandian, C. Viswanathan, S. Ramakrishna, RSC Adv. 5 (2015) 96416–96427.

[30] Y.R. Ma, C.M. Lin, C.L. Yeh, R.T. Huang, J. Vac. Sci. Technol. B Microelectron. Nanom. Struct. 23 (2005) 2141–2145.

[31] G.L. Frey, A. Rothschild, J. Sloan, R. Rosentsveig, R. Popovitz-Biro, R. Tenne, J. Solid State Chem. 162 (2001) 300–314.

[32] A. Baserga, V. Russo, F. Di Fonzo, A. Bailini, D. Cattaneo, C.S. Casari, A. Li Bassi, C.E. Bottani, Thin Solid Films 515 (2007) 6465–6469.

[33] S.H. Lee, H.M. Cheong, C.E. Tracy, A. Mascarenhas, D.K. Benson, S.K. Deb, Electrochim. Acta 44 (1999) 3111–3115.

[34] Y.C. Liang, C.W. Chang, Coatings 9 (2019).

[35] B. Abdel Samad, P. V. Ashrit, Thin Solid Films 636 (2017) 717–722.

[36] F. Wang, C. Di Valentin, G. Pacchioni, Phys. Rev. B - Condens. Matter Mater. Phys. 84 (2011) 1–5.

[37] S. Darmawi, S. Burkhardt, T. Leichtweiss, D.A. Weber, S. Wenzel, J. Janek, M.T. Elm, P.J. Klar, Phys. Chem. Chem. Phys. 17 (2015) 15903–15911.

[38] L. Berggren, A. Azens, G.A. Niklasson, J. Appl. Phys. 90 (2001) 1860–1863.

[39] C.A. Triana, C.G. Granqvist, G.A. Niklasson, J. Appl. Phys. 118 (2015).

[40] E. Salje, B. Güttler, Philos. Mag. Part B 50 (1984) 607–620.

[41] K. Miyake, H. Kaneko, Y. Teramoto, J. Appl. Phys. 53 (1982) 1511–1515.

[42] S.C. Moulzolf, S. an Ding, R.J. Lad, Sensors Actuators, B Chem. 77 (2001) 375–382.

[43] M. Regragui, M. Addou, A. Outzourhit, E. El Idrissi, A. Kachouane, A. Bougrine, Sol. Energy Mater. Sol. Cells 77 (2003) 341–350.

[44] J. Ederth, A. Hoel, G.A. Niklasson, C.G. Granqvist, J. Appl. Phys. 96 (2004) 5722–5726.

[45] H. Demiryont, Appl. Opt. 31 (1992) 250.

[46] G. Kim, H.J. Cho, Y.M. Sheu, H. Ohta, J. Phys. Chem. C 123 (2019) 15419–15424.

[47] Z. Hussain, Appl. Opt. 57 (2018) 5720.